A noninvasive method for measuring the velocity of diffuse hydrothermal flow by tracking moving refractive index anomalies

Eric Mittelstaedt, Anne Davaille, Peter van Keken, Nuno Gracias, Javier Escartin

Geochemistry Geophysics Geosystems G3

Article
Volume 11, Number 10
8 October 2010
Q10005, doi:10.1029/2010GC003227
ISSN: 1525-2027

Published by AGU and the Geochemical Society

A noninvasive method for measuring the velocity of diffuse hydrothermal flow by tracking moving refractive index anomalies

Eric Mittelstaedt and Anne Davaille
Fluides, Automatiques et Systèmes Thermiques Laboratoire, CNRS/UPMC/UPS, F-91405 Orsay CEDEX, France (mittelstaedt@fast.u-psud.fr)

Peter E. van Keken
Department of Geological Sciences, University of Michigan, Ann Arbor, Michigan 48109, USA

Nuno Gracias
EIA Department, University of Girona, Ed. PIV, E-17003 Girona, Spain

Javier Escartin
Institut de Physique du Globe de Paris, Université de Paris 6, F-75005 Paris, France

[1] Diffuse flow velocimetry (DFV) is introduced as a new, noninvasive, optical technique for measuring the velocity of diffuse hydrothermal flow. The technique uses images of a motionless, random medium (e.g., rocks) obtained through the lens of a moving refraction index anomaly (e.g., a hot upwelling). The method works in two stages. First, the changes in apparent background deformation are calculated using particle image velocimetry (PIV). The deformation vectors are determined by a cross correlation of pixel intensities across consecutive images. Second, the 2-D velocity field is calculated by cross correlating the deformation vectors between consecutive PIV calculations. The accuracy of the method is tested with laboratory and numerical experiments of a laminar, axisymmetric plume in fluids with both constant and temperature-dependent viscosity. Results show that average RMS errors are ~5%–7% and are most accurate in regions of pervasive apparent background deformation which is commonly encountered in regions of diffuse hydrothermal flow. The method is applied to a 25 s video sequence of diffuse flow from a small fracture captured during the Bathyluck'09 cruise to the Lucky Strike hydrothermal field (September 2009). The velocities of the ~10°C–15°C effluent reach ~5.5 cm/s, in strong agreement with previous measurements of diffuse flow. DFV is found to be most accurate for approximately 2-D flows where background objects have a small spatial scale, such as sand or gravel.

Components: 10,100 words, 11 figures.

Keywords: hydrothermal vents; diffuse flow; cross-correlation techniques; particle image velocimetry.

Index Terms: 3017 Marine Geology and Geophysics: Hydrothermal systems (0450, 1034, 3616, 4832, 8135, 8424); 3094 Marine Geology and Geophysics: Instruments and techniques; 0540 Computational Geophysics: Image processing.

Received 17 May 2010; **Revised** 26 August 2010; **Accepted** 31 August 2010; **Published** 8 October 2010.

Mittelstaedt, E., A. Davaille, P. E. van Keken, N. Gracias, and J. Escartin (2010), A noninvasive method for measuring the velocity of diffuse hydrothermal flow by tracking moving refractive index anomalies, *Geochem. Geophys. Geosyst.*, *11*, Q10005, doi:10.1029/2010GC003227.

1. Introduction

[2] Since the discovery of low-temperature hydrothermal venting along the Galapagos Spreading Center in the late 1970s [*Corliss et al.*, 1978; *Edmond et al.*, 1979], several methods have been introduced to estimate the heat flux associated with hydrothermal activity and the partition between diffuse and discrete venting. In general, these methods involve either direct point measurements at the site of diffuse venting using invasive flow collectors [e.g., *Ramondenc et al.*, 2006; *Sarrazin et al.*, 2009; *Schultz et al.*, 1992], or indirect methods that measure fluid properties (e.g., temperature) in the effluent plume after it buoyantly rises from the seafloor [e.g., *Rona and Trivett*, 1992] and/or is advected horizontally by ocean currents [e.g., *Trivett and Williams*, 1994; *Veirs et al.*, 2006].

[3] Estimates of diffuse heat fluxes at individual hydrothermal fields range from below the detection limit at the Rainbow vent field [*German et al.*, 2010] to ~2000 MW at the TAG hydrothermal field [*Rona and Trivett*, 1992]; a range that reflects interfield differences, temporal variability, scarcity of measurements, and uncertainty in measurement techniques. Published uncertainties in the diffuse heat flux, where stated, are commonly between ~50% and ~70% of the mean estimated heat flux [*James and Elderfield*, 1996; *Ramondenc et al.*, 2006; *Rona and Trivett*, 1992; *Trivett and Williams*, 1994]. Measurement scarcity is a significant source of uncertainty regardless of the measurement technique and can only be improved by further field studies with currently available techniques. Other sources of uncertainty for indirect methods include unconstrained plume sizes [e.g., *Trivett and Williams*, 1994], mixing of different vent sources [e.g., *Baker et al.*, 1993; *Ginster et al.*, 1994], unknown temporal variability of the diffuse flux at the source [e.g., *Scheirer et al.*, 2006; *Sohn*, 2007], and modeling assumptions [e.g., *Rona and Trivett*, 1992; *Trivett*, 1994]. For direct methods, sources of uncertainty often include the effect of invasive measurement devices on the flow [*Ramondenc et al.*, 2006; *Sarrazin et al.*, 2009; *Schultz et al.*, 1992], unknown flow variability with time [e.g., *Scheirer et al.*, 2006; *Sohn*, 2007], and extrapolation of small point-like velocity and temperature measurements to an entire vent field [e.g., *James and Elderfield*, 1996].

[4] In addition to the above sources of uncertainty, bathymetric variations and naturally occurring fauna can present difficulties for some direct measurement techniques. Direct measurement devices that use sensors in a vertical cylinder above a flow concentrator [*Sarrazin et al.*, 2009; *Schultz et al.*, 1992; *Schultz et al.*, 1996] can accurately measure fluid velocities (e.g., ±8% [*Schultz et al.*, 1992]). However, natural seafloor roughness and small fractures where diffuse flow is emitted [*Baker et al.*, 1993; *Rona and Trivett*, 1992] can prevent sealing between the seafloor and the flow concentrator. As noted by *Sarrazin et al.* [2009], a similar problem is also presented by biological communities of tube worms that are often found on or near diffuse flow sources.

[5] The above uncertainties and natural obstacles to current measurement methods suggest that a technique which is accurate, capable of surveying large areas of seafloor, can perform measurements on archived data, and is also flexible with regard to the terrain type will provide a useful addition to the already available methods. With this aim, we present a new optical technique, diffuse flow velocimetry (DFV), that measures the velocities of clear, diffuse, hydrothermal fluids by tracking of refractive index anomalies related to changes in fluid density (commonly due to differences in temperature and/or salinity). Here, we introduce the DFV method and demonstrate its accuracy in laboratory and numerical tests. We then discuss the applicability of DFV to diffuse hydrothermal flow, compare DFV to previous measurement techniques, and present an example calculation from a fracture at the Tour Eiffel vent site in the Lucky Strike hydrothermal field on the Mid-Atlantic Ridge.

2. Diffuse Flow Velocimetry

2.1. Laboratory Imaging of Index of Refraction Anomalies

[6] Variations in fluid density produce variations in refractive index [*Gladstone and Dale*, 1863] so that the trajectory of a light ray traversing an anoma-

lously dense fluid volume bends in the direction of increasing density. Objects viewed through the lens of such an index of refraction anomaly appear distorted (e.g., the "waves" seen above hot concrete on a summer day). There are a number of well-established measurement techniques that take advantage of this property. These include the schlieren laboratory technique [*Töpler*, 1866] and, recently, several correlation-based imaging techniques including "synthetic schlieren" [*Dalziel et al.*, 2000; *Sutherland et al.*, 1999] and "background-oriented schlieren" [*Meier*, 2002]. Synthetic and background-oriented schlieren are used both inside and outside of the lab to quantitatively measure variations in fluid density associated with, for example, moving helicopter blades [*Richard and Raffel*, 2001], the turbulent mixing of helium gas [*Meier*, 2002], sound waves from a gunshot [*Meier*, 2002], and an oscillating bar in a linearly stratified fluid [*Sutherland et al.*, 1999].

[7] DFV builds upon the above correlation-based methods which have their roots in the classical schlieren technique. Briefly, in the classic schlieren technique a knife edge is placed near the focal point of a parabolic mirror as an asymmetric aperture to block a fraction of previously collimated light after it traverses an index of refraction anomaly. Light intensity variations in the resulting image, due to bent light rays, are related to gradients in fluid density. Synthetic and background-oriented schlieren techniques measure variations in fluid densities without the need for the complicated mirrors and lighting of standard schlieren. The apparent shift of light rays passing through an index of refraction anomaly is calculated by cross correlating the image of a reference background (placed behind a uniform fluid at rest) with the resulting image when the background is seen through a density anomaly. The result is a 2-D field of apparent background deformation associated with density gradients in the fluid. In the case of a moving fluid, the apparent deformation field is displaced along with the density gradients. The new method presented here, diffuse fluid velocimetry (DFV), exploits the connection between the displacement of apparent background deformation and fluid movement to determine the 2-D velocity field.

2.2. Diffuse Flow Velocimetry Method

[8] We discuss DFV in the application of hydrothermal flow at the seafloor. Video sequences provide a series of images of a motionless, random medium (e.g., rocks) obtained through the lens of a moving refraction index anomaly (e.g., a hot upwelling) (Figure 1a). A DFV calculation involves two steps (Figure 2); the first determines the change in apparent deformation of subsequent background images and the second determines the movement of the apparent deformation through time to determine the fluid velocities. In the first step of the DFV method, the deformation field is determined using particle image velocimetry (PIV), for which we use the LaVision DaVis software (http://www.lavision.de/en/), as discussed by *Davaille and Limare* [2007] and *Limare et al.* [2008]. In the PIV calculation, a pair of consecutive images at times t_0 and t_1 are each divided into overlapping windows of L by N pixels. Here we use 8 × 8 to 32 × 32 pixels windows with an overlap of 50%. Using Fourier convolution, intensities at vertical pixel location l and horizontal pixel location n from a window at time t_0, $I_{\ln}^{t_0}$ are cross correlated with the spatially shifted window at time t_1, $I_{l+i,n+j}^{t_1}$, to create a correlation matrix C_{ij}

$$C_{ij} = \sum_{l=1}^{L} \sum_{n=1}^{N} I_{\ln}^{t_0} * I_{l+i,n+j}^{t_1}, \quad (1)$$

where the indices i and j correspond to vertical and horizontal pixel shifts of the window at t_1. The location of the maximum value in the correlation matrix corresponds to the highest probability displacement of the window caused by the refraction index anomaly between t_0 and t_1. This procedure is repeated for all windows and for all subsequent image pairs (i.e., t_0 and t_1, t_1 and t_2, …, t_{n-1} and t_n). The result is an instantaneous 2-D vector field of the change in the apparent background deformation due to movement of the index of refraction anomaly between each image pair (Figures 2d and 2e). For brevity, these changes in apparent background deformation are hereafter referred to as deformation vectors or, more generally, deformation.

[9] The deformation computed by DFV is different from that obtained by schlieren techniques where the correlation is performed in reference to a fixed, undistorted image. In DFV, the deformation vectors are computed from changes in the apparent background deformation between two subsequent images. This is essential in a hydrothermal environment where a reference image of the seafloor is unavailable due to continuous fluid flow. An estimate of the static background image can be

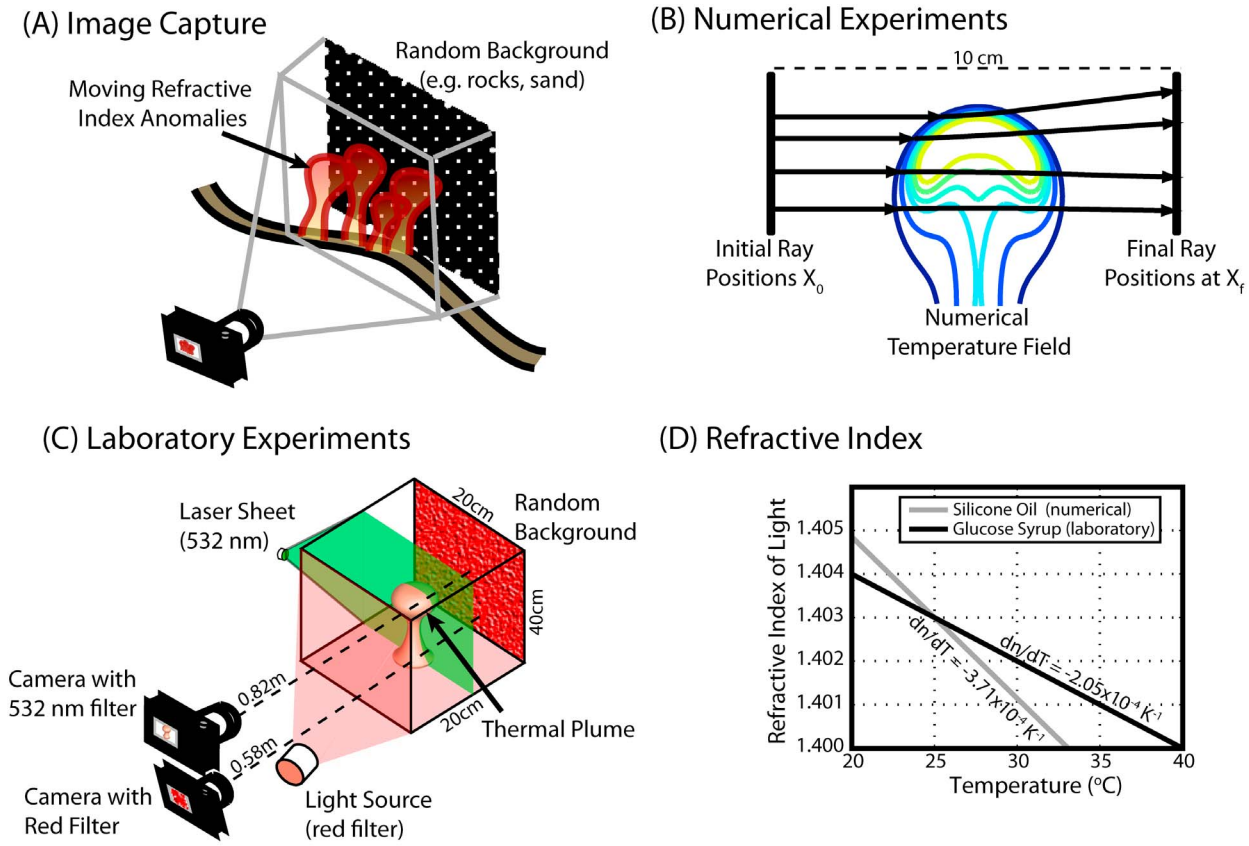

Figure 1. Diffuse flow velocimetry (DFV) calculates velocities from (a) a series of images of motionless, random media (e.g., rocks or sand) obtained through moving refraction index anomalies. Tests of DFV on an upwelling, laminar, axisymmetric plume are performed with (b) numerically distorted images created by shooting rays through numerical temperature fields and (c) images taken of a random dot pattern in the background of a laboratory tank. (d) Refraction index anomalies in both tests are caused by the linear relationship between index of refraction and temperature for silicone oil (numerical) and glucose syrup (laboratory).

obtained from the temporal median of pixel intensities, but is very prone to blurriness and loss of detail which degrade correlation accuracy.

[10] In a moving fluid, the deformation field moves a distance d between time $t_{0.5}$ and $t_{1.5}$ (the average times between t_0 and t_1 and t_1 and t_2 between which the deformation field is calculated as above). If we assume that in the small time between $t_{0.5}$ and $t_{1.5}$ the shape of the density gradients in the fluid remains nearly unchanged, d can be determined by cross correlation of the deformation vectors. In the second step of the DFV method, two subsequent deformation vector fields at $t_{0.5}$ and $t_{1.5}$ are each divided into overlapping windows of L by N deformation vectors. We use windows of 8 × 8 vectors with a 50% overlap. For a single window, the correlation matrix D_{ij} is defined to be a function of both the horizontal and vertical components, X and Y, of the deformation vectors

$$D_{ij} = \sqrt{\frac{\sum_{l=1}^{L}\sum_{n=1}^{N}\left(X_{\ln}^{t_{0.5}} - X_{l+i,n+j}^{t_{1.5}}\right)^2}{L * N}} + \sqrt{\frac{\sum_{l=1}^{L}\sum_{n=1}^{N}\left(Y_{\ln}^{t_{0.5}} - Y_{l+i,n+j}^{t_{1.5}}\right)^2}{L * N}}, \quad (2)$$

where l and n are the local vertical and horizontal window coordinates of a deformation vector, and i and j are the vertical and horizontal window vector shifts. The location of the minimum of D_{ij} defines the highest probability displacement vector d of the window between $t_{0.5}$ and $t_{1.5}$. The precision of the location of the

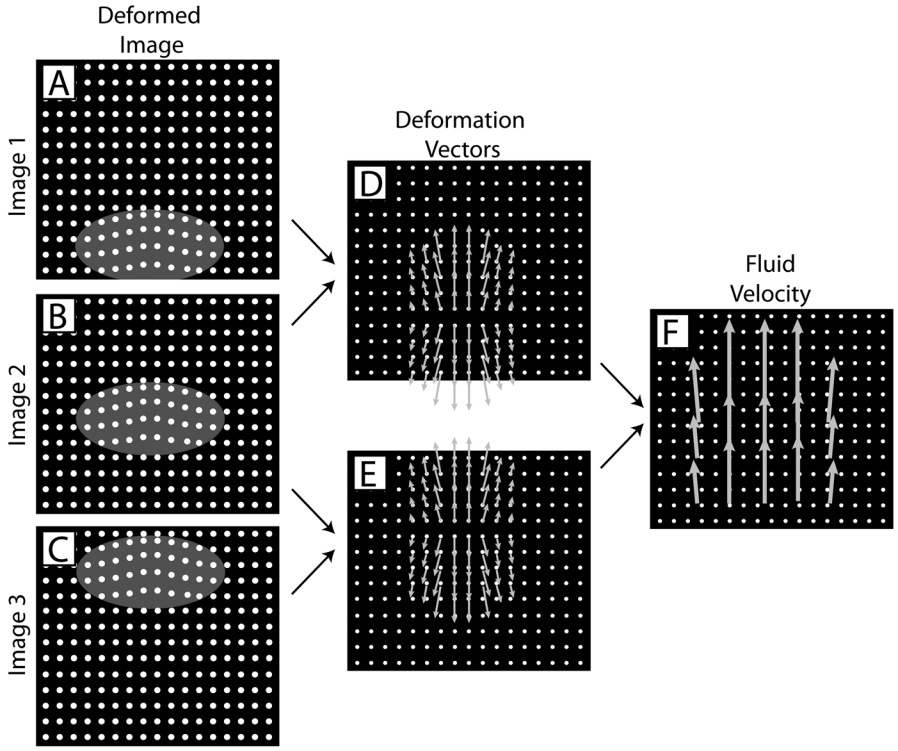

Figure 2. A cartoon representation of the steps involved in DFV. (a–c) Apparent deformation of a background in subsequent images is captured through the lens of a refractive index anomaly (ellipses). (d and e) The change in the apparent background deformation is calculated between these images (vectors). Finally, the location of the calculated deformations is tracked between calculations to yield (f) the fluid velocities (vectors).

correlation minimum is improved from ±0.5 times the distance between vector locations to ~±0.1 times the intervector distance with an analytical three-point Gaussian fit in both coordinate directions [*Willert and Gharib*, 1991]. The use of the Gaussian fit is motivated by its rapid calculation and its low interpolation errors in PIV applications [*Roesgen*, 2003]. The displacement vector d yields a velocity vector for the given window

$$\vec{v} = \frac{d_x \cdot p_x \cdot S}{(t_{1.5} - t_{0.5})}\hat{x} + \frac{d_y \cdot p_y \cdot S}{(t_{1.5} - t_{0.5})}\hat{y}, \quad (3)$$

where p_x and p_y are the horizontal and vertical number of pixels between each deformation vector, S is the ratio of centimeters to pixels, and $\vec{v}$ is the velocity vector in cm/s at time t_1. The cross correlation is performed on all the windows to yield the instantaneous, 2-D velocity field (Figure 2f).

[11] The location of the correlation minimum in equation (2) gives the highest probability displacement of the deformation field in the window, but outliers can occur due to poor image quality, little or no fluid movement, and/or undetectable deformation (due to very small, very large, or nonexistent density variations). Three methods are used to limit false correlations. First, the velocity is considered valid only if the curvature in the immediate neighborhood of the correlation minimum is greater than an empirically determined critical value of 1×10^{-3} to 1×10^{-4}. Second, a correlation minimum is considered invalid if it falls on the boundary of the correlation matrix. If a correlation minimum does not have a sufficient curvature or falls on the edge of the correlation matrix, it is assumed to be erroneous and the velocity in that location is set to 0. Finally, the calculated velocities are smoothed by a 3 × 3 median filter. Although some accurate velocities are eliminated, the combination of these three methods effectively reduces the number of highly inaccurate velocities (Figure 3). The above methods for eliminating false correlations produce similar results to methods using a local roughness criteria [e.g., *Crone et al.*, 2010].

[12] Two sets of Matlab code are provided to facilitate the above DFV calculations (auxiliary

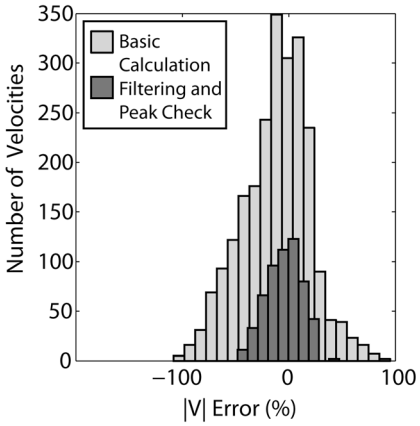

Figure 3. The straightforward correlation of deformation vectors produces velocities that can have large errors (light gray bars), but the use of filtering and ensuring a minimum curvature in the correlation minimum effectively eliminates the most erroneous vectors (dark gray bars).

material).[1] The first calculates the apparent changes in background deformation between images and is a slightly modified version of OpenPIV (http://www.openpiv.net/). Although we use the proprietary DaVis software to perform PIV calculations here, final DFV velocity fields are comparable when using OpenPIV. The second is the DFV code used by the authors to calculate fluid velocities from deformation vectors.

3. Experimental Tests

[13] The accuracy of DFV velocities is tested using two experiments. The first is based in the laboratory and the second uses a numerical model based upon a similar laboratory setup. In both experiments, a thermally buoyant, axisymmetric, laminar plume produces the required refractive index anomaly (Figures 1b and 1c). To introduce the upwelling plume, a fluid (sugar syrup in the laboratory and silicone oil for the numerical method) is heated from below by a localized, circular heat source. The temperature gradient between the plume and the ambient fluid produces refraction index gradients that distort images of a random (laboratory) or regular (numerical) dot pattern behind the plume. In the laboratory, images are captured using a red-filtered light source and camera. We use ray tracing to construct synthetic images from the numerical results. Images of the distorted backgrounds are used to calculate fluid velocities with DFV. The results are compared with known plume velocities (laboratory PIV velocities and numerical model velocities). For a full description of the experimental methods see Appendix A.

[14] Values of the Rayleigh and Prandtl numbers in our experimental tests (Ra ~$10^{3–4}$; Pr ~10^{4}) differ from those expected in diffuse hydrothermal systems (Ra ~$10^{5–6}$; Pr ~10^{1}). However, these numbers describe dynamical conditions of the flow, not the magnitude of apparent background deformation critical to DFV measurements. A more relevant value is the theoretical scale of apparent background deformation (Appendix B)

$$\left(\frac{\Delta p}{h}\right) = \frac{-2d_B\Delta T}{hn_{ambient}}\frac{\partial n}{\partial T},$$

where h is the characteristic half-width of the index of refraction anomaly, Δp is the vertical shift of a light ray from horizontal, and d_B is the distance between the anomaly and the image capture device (Figure 5). Values of $\Delta p/h$ range from 0.1 to 2.1 in our experiments and are estimated to be ~0.5–0.6 for the example of hydrothermal diffuse flow in section 5.4, within the range of our experimental conditions (Figure B1).

4. Results

4.1. Observed Patterns of Apparent Background Deformation

[15] The nearly identical setups of the numerical and laboratory experiments produce similar patterns of deformation (Figures 4b and 4e). Note, however, that the sign of the deformation in the laboratory images is reversed with respect to the numerical results discussed below due to the different optical focus plane locations (Figure 5). This difference does not affect the DFV calculation. Initially, formation of a conductive thermal boundary layer at the base of the tank or numerical domain produces very strong temperature gradients that distort the background image to the point of being unrecognizable (i.e., deformations cannot be successfully calculated in this region). After convective motions begin and the upwelling leaves the boundary layer, the temperature gradients decrease and are largest on the edges of the rising plume head and tail (i.e., between the warm, upwelling plume and the cooler, ambient fluid). Around the plume head, deformations form two horseshoe-shaped regions, one just above the other with the lower region appearing to deform in the negative

[1] Auxiliary materials are available in the HTML. doi:10.1029/2010GC003227.

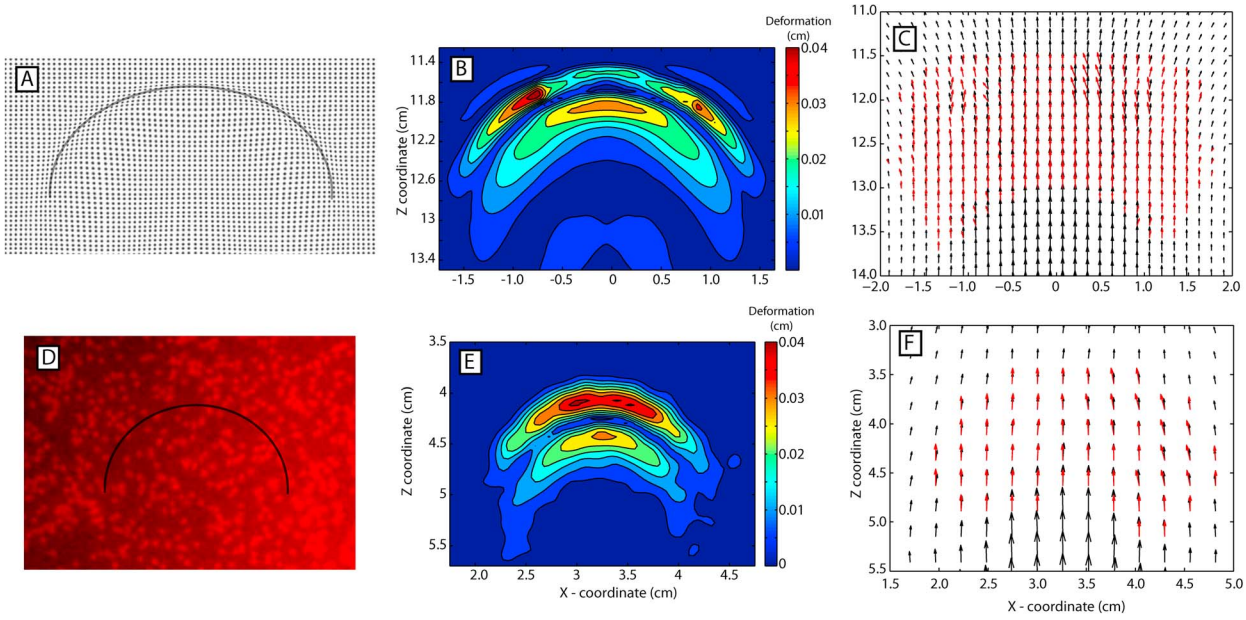

Figure 4. An upwelling thermal plume acts as a refraction index anomaly causing an apparent distortion of (a) a numerically produced grid (t = 100 s) and (d) the background of a laboratory tank (t = 110 s). The calculated deformation magnitudes of the (b) numerical and (e) laboratory background are on the order of 0.01 cm. The DFV velocities (red arrows) are calculated by cross correlating the deformation field between successive calculations and are compared with (c) numerical velocities (black arrows) or (f) PIV velocities (black arrows) of particles imaged in the flow.

direction and the upper region in the positive direction (Figure 4b). The inversion in the sign of deformation is caused by the divergent refraction anomaly initially "moving" the background image upward and outward (positive deformation) and the subsequent return of the image to a less distorted state, moving downward and inward (negative deformation), as the anomaly passes (Figures 2d, 2e, 6a, and 6b). The magnitude of the background deformations in the plume head region is on the order of 0.01 cm, but is zero in the plume stem after it achieves a steady state temperature structure. As the plume head continues to rise, the magnitude of the deformations decreases with the decreasing temperature anomaly (Figures 6a and 6b). This suggests that the anomaly will become undetectable, although at a scale height larger than that seen in our experiments. Overall, we see less uniformity in the numerical deformation pattern than that of the laboratory experiment, in part due to discretization errors in the generation of the numerical images (auxiliary material).

4.2. Advection, Diffusion, and Fluid Velocities

[16] The DFV velocities of the thermal plume in our experiments are not equal to particle velocities within the fluid, but are due to a combination of fluid advection and thermal diffusion. Centerline profiles (i.e., along the vertical plume axis) of the vertical temperature gradient (dT/dz), the vertical deformation, and contours of temperature from the numerical experiment at four times ($t1$, $t2$, $t3$, and $t4$) show that the height of the maximum and

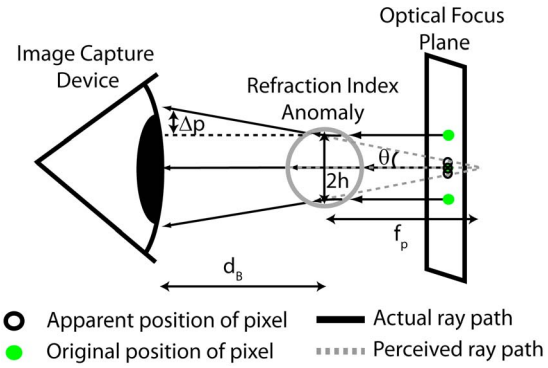

Figure 5. The original positions of pixels (green dots) seen through a divergent refraction index anomaly appear to move toward each other (black circles) due to the location of the optical focus plane. The numerical experiment calculates the position of the light rays at the location of the image capture device and, thus, displays the opposite pixel motion. See Appendix B for a description of parameters.

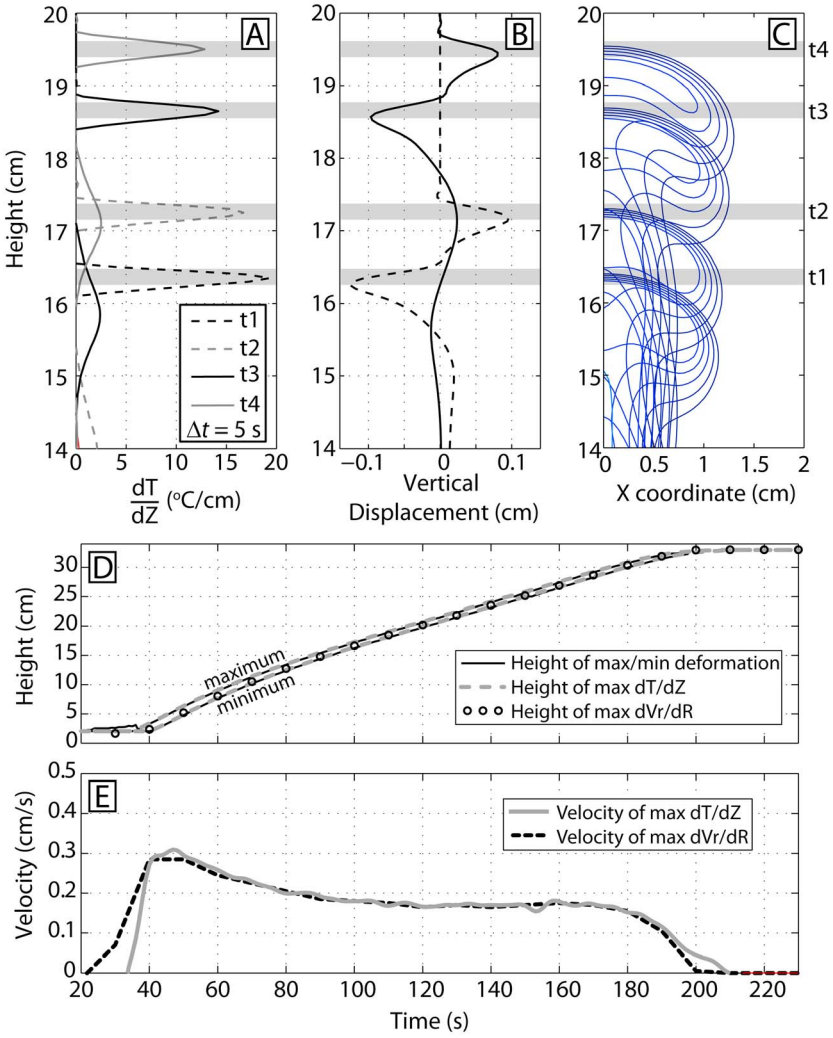

Figure 6. Centerline profiles of (a) the vertical temperature gradient at four times t_1 (black dashed line), t_2 (gray dashed line), t_3 (solid black line), and t_4 (solid gray line); (b) calculated deformation between t_1 and t_2 (dashed line, Δt = 5 s) and t_3 and t_4 (solid line, Δt = 5 s); and (c) isotherms at each time show that the locations of deformation extremes lie just below the locations of the maximum temperature gradients (gray bars). (d) The relative location of the deformation extremes (gray dashed lines) and the maximum vertical temperature gradients (black lines) is nearly constant. The deformation extremes also lie below the location of the plume head stagnation point where the radial velocity gradient is a maximum. (e) For most of the experiment, the velocity of the stagnation point (black line) and the maximum vertical temperature gradient (gray line) are almost identical.

minimum deformations between *t1* and *t2* and between *t3* and *t4* (Δt = 5 s) fall just below the heights of the maximum temperature gradients (dT/dz) at each time (Figures 6a–6c). The relative positions of the maximum dT/dz, controlled by advection and thermal diffusion, and the extremes in deformation are constant throughout nearly the entire risetime of the upwelling plume (Figure 6d), indicating identical velocities. The contribution of thermal diffusion is reinforced by a common laboratory measure of plume head velocity; the movement of the stagnation point at the top of the plume head where the radial velocity gradient dV_r/dr is a maximum. For similar experimental fluids, the velocity of the stagnation point is previously shown to include advection as well as conductive expansion of the plume head [*Davaille et al.*, 2010]. The location of the stagnation point in our numerical model is slightly above the location of the maximum temperature gradient and between the extremes in deformation throughout the risetime of the plume (Figures 6d and 6e). Thus, the velocity of the

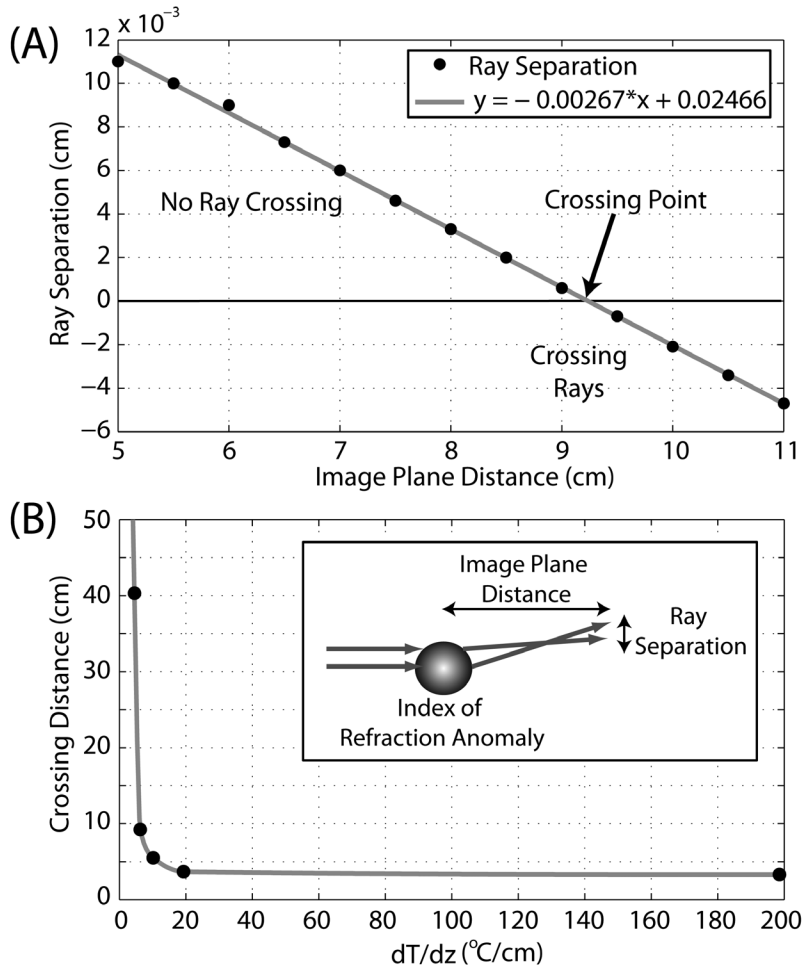

Figure 7. (a) The distance between two initially parallel rays (black dots, ray separation, negative if the rays cross) shot through the numerical thermal field is linearly related (gray line) to the distance (measured from the plume center) to the image plane. If the rays exit the plume at slightly different angles, they may cross (crossing point, ray separation = 0). (b) The distance from the plume center to the ray crossing (black dots) is a strongly nonlinear function of the vertical temperature gradient at the ray location as it crosses the plume center.

extremes in deformation (i.e., the DFV velocity) is identical to the velocity of the stagnation point.

4.3. Image Distortion and Ray Crossings

[17] Two closely spaced, parallel rays traversing a fluid volume with large gradients in refractive index may bend to slightly different degrees and eventually cross after they have left the anomalous fluid. Crossing light rays may partially obscure background images and add noise to deformation calculations. To examine this possibility, we shoot two initially parallel rays (Appendix A), separated vertically by 0.025 cm, through the center of the plume axis and examine the final ray separations at different distances beyond the plume center (Figure 7a). After leaving the thermal anomaly, the index of refraction remains constant and the ray separation is a linear function of distance from the plume center. For cases where the rays cross, the vertical temperature gradient in the plume center (at the height of the ray) is used as a proxy for the intensity of the index of refraction gradients along the ray trajectory (Figure 7b). Ray crossing distance is a strongly nonlinear function of the vertical temperature gradient with distances between 3.3 cm and 40.3 cm for vertical thermal gradients of between 198.6°C/cm and 4.51°C/cm. The crossover distances for similar thermal gradients in seawater are likely to be larger because the temperature dependence of the index of refraction is approximately one third that of silicone oil ($dn/dT = \sim -0.9 \times 10^{-4}$ K^{-1} best fit for seawater between 5°C and 30°C at a wavelength of 589 nm [*Quan and*

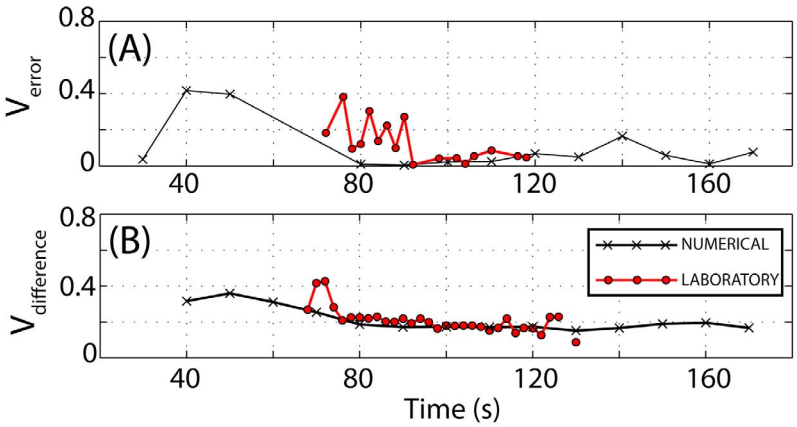

Figure 8. Misfit between DFV calculated velocity and the (a) stagnation point velocity scaled by the stagnation point velocity and (b) the RMS difference between the DFV velocities and material velocities scaled by the maximum velocity. The DFV velocities are compared to both numerical (black crosses) and laboratory PIV velocities (red circles).

Fry, 1995] and $dn/dT = -3.71 \times 10^{-4}$ K^{-1} for silicone oil).

4.4. Misfit in Experimental DFV Velocities

[18] The DFV velocity vectors represent an average velocity of the thermally induced refraction index anomaly within each window. For the conditions of our experiments, the difference between this velocity and the velocity of particles within the fluid is ~5%–10% [*Davaille et al.*, 2010] (section 4.2). Thus, the particle velocities are a poor metric for quantitative errors in the DFV calculations. Instead, quantitative errors are determined using the stagnation point velocity, which moves with the refractive index anomaly (section 4.2). The stagnation point velocity, however, only provides error measurements at a single location and the differences between the numerical and laboratory PIV and the DFV velocities are still used for qualitative discussion of the error.

[19] Quantitative errors are calculated by finding the misfit between the stagnation point velocity and the DFV velocity interpolated to the same location and scaled by the stagnation point velocity (Figure 8a). The misfit for the numerical cases varies from 0.005 to 0.418 and for the laboratory cases from 0.008 to 0.382. The RMS error of all the numerical measurements is 0.1705 and for all the laboratory measurements is 0.1656.

[20] During the initial stages of plume upwelling the errors tend to be high, but later settle to a lower level (Figure 8a). This may be due to the initially high temperature gradients (i.e., large background deformations) in the plume head as it leaves the thermal boundary layer (auxiliary material). In the numerical experiment, the RMS error after and including 80 s is 0.067, a decrease of 0.104 from the overall value. In the laboratory, the RMS error after and including 90 s is 0.05, a decrease of 0.116. These lower values are more representative of the level of error seen in the established flow during the majority of the experiments (70% of the numerical experiment and 56% of the laboratory experiment).

[21] More qualitatively, the DFV velocities can be compared with local spatial averages of the numerical or PIV values within the area of each window. In general, the DFV and the locally averaged numeric and PIV vectors closely resemble one another with many vectors nearly completely overlapping (Figures 4c and 4f). For a given time, we calculate the root-mean-square (RMS) difference between the total velocities V of the DFV and the numerical or laboratory calculations scaled by the maximum velocity (Figure 8b). For the numerical experiment, the RMS differences are between 0.1511 and 0.359 and for the laboratory experiment are between 0.087 and 0.426. As for the comparison with the stagnation point velocity, an initially high difference is followed by a decrease to a lower level. In the numerical experiment, the temporally averaged RMS error is 0.213, but taking only the values after and including 80 s, it falls to 0.174 (decrease of 0.04). Similarly, the average RMS difference over all time from the laboratory experiment is 0.208, and after 78 s it becomes 0.188 (decrease of 0.02).

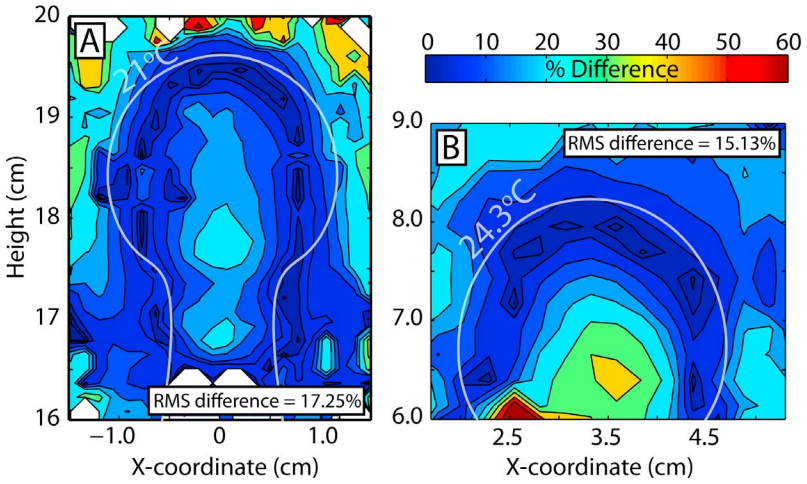

Figure 9. Contour plots of the difference between the magnitude of DFV velocities and numeric or PIV velocities as a percentage of the maximum velocity for (a) the numerical and (b) the laboratory tests. A region of very small differences (<10%) approximately contours the shape of the plume isotherms (white lines).

4.5. Spatial Distribution of Error

[22] Although the numerical and PIV laboratory velocities are not identical to the motion of the refractive index anomaly (section 4.2), their difference from the DFV velocities demonstrates the expected spatial distribution of error. Figure 9 shows the percent difference of the total velocity scaled by the maximum numerical or PIV vertical velocity for a single time step (t = 130 s, numerical, t = 110 s, laboratory). To better evaluate the spatial variation of the difference, no curvature limit of the correlation minimum (equation (2)) is used to eliminate bad correlations in Figure 9, but smoothing is still performed (section 2.2). A ring (numerical) or horseshoe (laboratory) of velocity differences of <10% approximately contours the shape of the rising plume head. The velocity differences reach values of ~20% for the numerical experiments and reach ~35%–40% for the laboratory within the center of the plume head. Finally, the misfits reach 50%–60% in both the numerical and laboratory experiments in the regions external to the plume head.

5. Discussion

5.1. Sources of Experimental Error

[23] Errors in our experimental tests are largest in the initial stages of plume growth due to large temperature gradients in the thermal boundary layer that cause crossing and diverging rays (sections 4.3 and 4.4), but other factors are also predicted to contribute to the observed errors. In the laboratory tests, imaging of the background was difficult due to low light levels caused by the red filters used. Additionally, uneven lighting in the laboratory (brighter on the right-hand side) may also contribute to errors in the DFV velocities. In the numerical tests, a potential source of error is the noise in the simulated images due to interpolations, numerical errors, and a finite number of rays.

[24] Another possible source of error, and a difficulty with all optical techniques, is the 3-D nature of the flow. The apparent background deformation is caused by the integrated effect of the refraction index gradients along each raypath. Slower, cooler portions of the plume upwelling may be expected to effect the DFV velocities. However, the small errors associated with the stagnation point velocity (Figure 8a) and the coincidence of the peak deformation and the peak vertical thermal gradient along the plume axis (Figures 6a and 6b) suggest that DFV is most sensitive to the maximum upwelling velocity (i.e., largest temperature gradient) at each location (section 4) and is rather insensitive to the 3-D nature of the upwelling plume. Despite this, a more complicated 3-D flow structure may introduce some error in the DFV calculation.

5.2. Applicability to Diffuse Flow at Hydrothermal Vents

[25] Along-axis, diffuse hydrothermal flow is driven primarily by thermally induced convection within the upper crust [*German and Von Damm*, 2003; *Ingebritsen et al.*, 2010] and is often mild-

ly turbulent with multiple individual upwellings (see auxiliary material). This type of flow creates variable temperature gradients throughout the upwelling effluent and pervasive distortion of objects behind the flow. In our experimental results, regions of the flow with large thermal gradients (e.g., around the border of the plume head) produce significant background deformation which result in small differences between the particle and DFV velocities (<10%, Figure 9). This suggests that errors in DFV velocities of diffuse hydrothermal flow are likely to be on the lower end of the RMS errors observed in our experimental tests.

[26] The DFV calculation is insensitive to the cause of the refractive index anomaly (e.g., anomalous temperature and/or salinity) and is predicted to calculate accurate fluid velocities as long as the refractive index anomaly and the fluid move together. This is not always the case. In our experimental tests, conductive expansion of the rising plume head (section 4.2) contributes to the DFV velocities. For the high Prandtl number fluids used in our experimental tests (silicone oil and glucose syrup, $Pr \sim 10^4$), this effect can be attributed to different thicknesses of the velocity and thermal boundary layers [*Davaille et al.*, 2010], but water has a much smaller Prandtl number ($Pr \sim 10$) and the boundary layer thicknesses will be similar. In addition to thermal effects, the vorticity in turbulent diffuse flow causes particles to move around in eddies, but the refractive index anomaly moves with the mean flow. Thus, DFV velocities of diffuse flow in seawater are not strongly affected by thermal diffusion and are a measure the mean fluid flow.

[27] The size and intensity of objects in the background of video sequences of diffuse flow at hydrothermal vents can affect the accuracy of DFV calculations. Our experiments use a regular grid or random distribution of small dots to provide a background where deformations are easily tracked using standard PIV algorithms. On the seafloor, similar patterns are found in areas with gravel, sand, rocks, or small immobile fauna of variable color. Large, uniform intensity rocks or shells hamper the calculation of background deformation and, thus, the DFV velocities. Velocities from portions of an image with large objects of uniform intensity should not be considered as representative of the overall fluid velocity.

[28] The DFV method is most effective for diffuse hydrothermal flow that is optically thin, such as flow from linear fractures, and for immobile background patterns. It is difficult to properly measure the apparent background deformation across a large surface where diffuse flow is pervasive (e.g., a biological mat). This difficulty can be overcome by a synthetic background pattern (e.g., a board placed on the seafloor or held by an ROV) which can isolate optically thin slices of the fluid. In the case of rapid, variable background movement (e.g., tube worms in a current), DFV calculations can be performed on short video segments during periods of background stability (e.g., a lull in the current) without the aid of an artificial background. Otherwise, a synthetic background is necessary to perform measurements in front of a constantly moving natural background.

[29] Buoyant diffuse flow will rise vertically in a steady environment, but is often forced laterally by ocean currents. If this lateral flow is into or out of the plane of the video images, it does not contribute to the 2-D, DFV velocity field. This can be avoided by orienting the camera perpendicular to the prevailing ocean current direction. However, if the desired measurement is the diffuse heat flux, a reasonable measurement can be achieved, regardless of the current, by isolating the vertical component of the fluid flow.

5.3. Comparison of Diffuse Flow Velocimetry to Previous Methods

[30] Previous methods for measuring diffuse hydrothermal flow, including visual particle tracking and flow collector type mechanical/electrical measurements, have several shortcomings. Potential problems associated with visual tracking of particles in video sequences include a lack of particles in a given flow, a low spatial resolution within the flow, a low temporal resolution due to gaps in the passage of particles, and turbulent fluid flow that causes particle motions to deviate from the mean flow of the fluid yielding incorrect velocities. Shortcomings associated with flow collector type measurements include very small spatial resolution (a single point), the need for a specially designed and built mechanical device with electronics that could potentially fail, the inability to seal the flow collector to the seafloor, difficulty performing long-term monitoring [e.g., *Crone et al.*, 2010], and possible changes to the fluid flow due to the presence of the device.

[31] DFV has several advantages over visual particle tracking and flow concentrator techniques. First of all, DFV can be used to calculate fluid

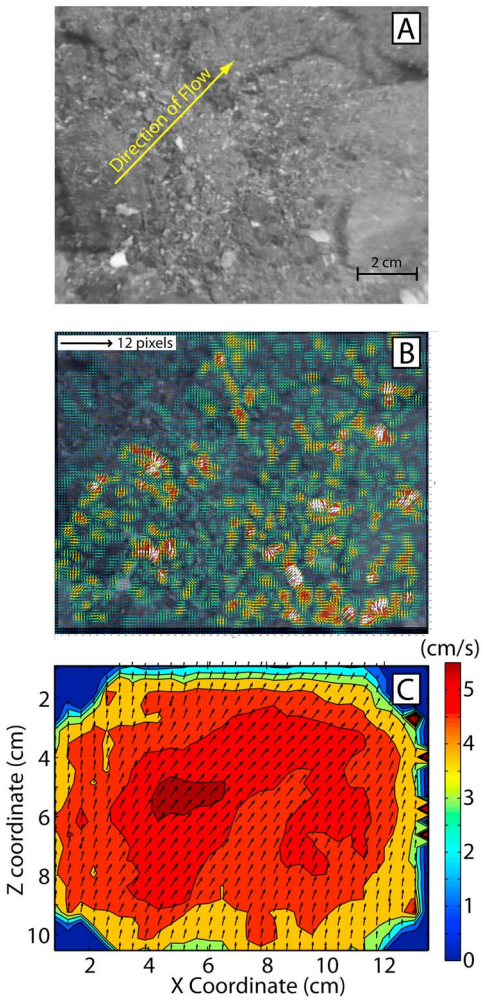

Figure 10. (a) A 25 s video sequence of the seafloor, seen through the lens of moving refractive index anomalies associated with ~10°C–15°C diffuse effluent, is used to calculate (b) the apparent background deformation between every fifth image (hotter colors for larger magnitudes). (c) The time-averaged velocities reach a maximum of ~5 cm/s. The video sequence was taken in September 2009 during the Bathyluck expedition to the Lucky Strike hydrothermal field along the Mid-Atlantic Ridge.

velocities on archived video data. Video from previous ROV or submersible dives on hydrothermal sites can be scanned for appropriate sequences and used to estimate the diffuse flow velocities. Thus, significant increases in measurement number and density can be achieved without additional field studies. In addition, because many of the best suited image sequences are captured when temperature sensors are installed, a corresponding temperature is likely to be available for heat flux calculations. Another advantage is that no special measuring devices or electronics are required for DFV measurements (however, see section 5.5). In contrast to previous methods with low spatial resolution, across the seafloor and/or in the flow itself, DFV produces 2-D velocity fields 10–20 cm (or greater) across with a spatial resolution of <1 cm to a few centimeters. DFV thus can provide improved understanding of flow structure, and temporal and spatial flow variation across a hydrothermal field. Long-term monitoring of diffuse flow using DFV is limited only by the video length, and is unlikely to suffer equipment failure associated with mineral precipitation, high temperatures, or low pH fluids [see *Crone et al.*, 2010]. Finally, DFV can quickly survey a large area of hydrothermal diffuse flow; each velocity calculation requires only ~1 min of video.

5.4. Example: Diffuse Flow From a Fracture at the Tour Eiffel Vent Site, Lucky Strike Hydrothermal Field

[32] During the recent Bathyluck'09 expedition to the Lucky Strike hydrothermal field (September 2009) aboard the French research vessel *Pourquoi Pas?* (IFREMER), a video survey of diffuse flow was performed along a series of fractures surrounding the Tour Eiffel vent site. Here, we present an example of buoyantly rising diffuse flow from one such fracture in a 25 s video sequence captured by the main camera on the ROV *Victor 6000*. The flow temperature of ~10°C–15°C is measured by placing the ROV's onboard temperature probe in the diffuse upwelling. The probe is also used as an image scale. The camera is focused on the sandy background and the image frame is placed just above the fracture opening (Figure 10a) with a downward camera angle of 38° from horizontal. To provide a stable imaging platform, the ROV is placed directly onto the seafloor near the fracture of interest. Despite this precaution, variations in the bottom current shift the ROV and cause constant camera movement. The camera system records 50 frames per second interlaced video at a resolution of 720 × 540 (~0.027 cm/pix). To prepare the video images for DFV calculations, the sequence is deinterlaced and the camera motion is removed by a robust feature matching algorithm [*Gracias*, 2003]. Apparent background deformations are calculated between every fifth image (i.e., $\Delta t = 0.1$ s) with square image windows 8 pixels to a side (Figure 10a). The correlation of the deformation pattern is calculated between each deformation field

on square windows of 8 deformation vectors to a side. At the location of each calculated velocity vector, a time average (through all 25 s of video) is calculated including all velocities within 2 standard deviations of the maximum velocity at that vector location (Figure 10c). These limits avoid inclusion of 0.0 cm/s velocities associated with bad correlations (section 2.2).

[33] Around the edges of the image frame, there is a decrease in the calculated velocities. This apparent edge effect is caused, in part, by the contouring program. In the upper left-hand corner there is a triangular region of slow velocities which appears accurate as very little flow is observed in this location (auxiliary material). Very slow velocities in the remaining image frame corners may be associated with uncorrected distortion caused by the camera optics. In the bottom right-hand portion of the frame, a large, uniformly colored rock may be expected to disrupt the deformation calculation and cause noisy correlations, but velocities are similar to the rest of the velocity field (Figure 10c). Tests indicate that DFV velocities are unchanged near the edge of a calculation which suggests that the observed decrease in velocities is unlikely to be due to the DFV method.

[34] The calculated deformation pattern and time-averaged DFV velocities agree well with our experiments, the fluid motion in the video sequence (Figure 10a; see auxiliary material), and with previous measures of diffuse flow. Deformation patterns due to plume-like structures in the flow have a double-horseshoe shape with oppositely oriented distortions (Figure 10b, middle left part of image) similar to that seen in our experimental tests (Figure 4). The time-averaged DFV velocities (after correction for the downward angle of the camera) are up to ~5.5 cm/s in a direction up and to the right in the frame of the image. The magnitude of the calculated velocities is in good agreement with previous estimates of diffuse flow rates from fractures, such as at the East Pacific rise where *Ramondenc et al.* [2006] find diffuse flow rates of 3–5 cm/s for a fluid temperature of 10°C and at the Endeavor segment of the Juan de Fuca Ridge where *Schultz et al.* [1992] find diffuse flow velocities of ~7–15 cm/s for fluids of 7°C to 13°C. The fracture-based measurements are approximately an order of magnitude greater than the velocities from biological mats which range from ~0.1–1 cm/s [*Ramondenc et al.*, 2006; *Sarrazin et al.*, 2009]. These results show that DFV can successfully measure the time-averaged 2-D velocity field of diffuse effluent within an image frame ~10–20 cm across using only standard ROV video.

5.5. Future Improvements to DFV

[35] Future improvements to the DFV method aim to improve measurement sensitivity, accuracy, and versatility. Although DFV can successfully measure fluid velocities using a seafloor background (section 5.4), measurement accuracy will likely be improved through use of a synthetic background attached to a separate, calibrated camera system, similar to our laboratory and numerical experiments. Implementation of a synthetic background with a known size, shape, and pattern will expand the number of locations where DFV can be performed, will allow for correction of camera lens distortion, and will provide an accurate image scale (pixels to distance). In addition, a known background may allow synthetic schlieren measurements to be used to calculate the 2-D field of fluid density [e.g., *Dalziel et al.*, 2000]. Coupled with a few point measures of temperature, the 2-D density field can be used to calculate the 2-D salinity and thermal fields. DFV accuracy is also limited by motion of the ROV camera during image acquisition (overcome here with numerical processing). Attachment of the synthetic background to a separate camera system will eliminate stabilization issues. A further benefit of a separate camera and background system will be the ability to perform other actions with the ROV during video capture as well as to perform long-duration measurements to study diffuse flow variability.

6. Conclusions

[36] We present a new optical method for calculating the velocity of diffuse hydrothermal flow, diffuse flow velocimetry (DFV). DFV calculates velocities of clear fluid flow by tracking changes in apparent background deformation caused by moving refraction index anomalies. Numerical and laboratory tests of DFV on an upwelling, laminar, axisymmetric plume yield errors between 0.5% to 41.8% and average values of 5%–7% after the plume reaches a few centimeters above the thermal boundary layer. Spatial variations in the differences between particle and refraction index anomaly velocities suggest that errors are small in areas of the flow with significant apparent background deformations, such as in regions of diffuse hydrothermal flow where there is pervasive dis-

tortion of the image background. Sources of potential error in the DFV calculation include large background objects of uniform color, poor lighting or image resolution, an unstable platform (e.g., a moving ROV camera), 3-D flow structure, out-of-plane fluid motion, and very large thermal gradients that may prevent calculation of the background deformation. Many of these shortcomings can be overcome with the use of an artificial background placed behind the flow. DFV velocities of diffuse effluent rising from a fracture at the Tour Eiffel vent site in the Lucky Strike hydrothermal field on the Mid-Atlantic Ridge show strong agreement with previous measurements along the East Pacific Rise and Juan de Fuca Ridge. The DFV method allows accurate measurement of diffuse flow velocities on both new or archived video data without specially designed equipment and is capable of rapidly surveying large regions of diffuse hydrothermal flow.

Appendix A: Experimental Methods

A1. Laboratory Experiment

[37] To initiate an upwelling, laminar plume in the laboratory, a Peltier device is placed at the bottom of a Plexiglass tank (20 cm × 20 cm × 40 cm) filled with glucose syrup that is seeded with 10 μm glass microspheres. Heating is initiated by placing a voltage (4 W) across the Peltier device. The resulting thermal upwelling produces a refractive index anomaly (Figure 1d, glucose, $dn/dT = -2.05 \times 10^{-4}$ K^{-1}) as it rises through the tank.

[38] Two light sources illuminate the flow. A vertically oriented 532 nm (green) laser sheet aligned along the axis of symmetry of the plume and perpendicular to the view direction provides backscatter from the glass microspheres. A diffuse light source illuminates a background pattern through a red 091 B+W camera filter. The background consists of randomly distributed 0.3 mm diameter white dots (Figures 1c and 4d). PIV performed on images of the backscatter from the laser-illuminated glass microspheres yields the material velocities which are used for error calculations (section 4.4). Previous work demonstrates that errors in PIV velocities for this experimental setup are nonnegligible, but small (<5%) [*Davaille et al.*, 2010]. Images of the laser sheet are captured using a CCD camera with a 532 nm filter at a distance of 0.82 m from the back of the tank, at a height of 121 cm (approximately equal to the height of the plume), at a rate of 2 Hz, and a resolution of ~0.018 cm/pixel. Background images are captured with a separate, red-filtered (identical to the light source filter) CCD camera at a distance of 0.58 m from the back of the tank, at a height of 111.5 cm, and upward angle of 4.39°, a rate of 0.5 Hz, an exposure time of 0.1 s, and a resolution of ~0.011 cm/pixel. The DFV and PIV calculations are performed in a region between 2 cm and 14.35 cm above the Peltier device and between 6.47 cm and 13.19 cm from the left-hand edge of the box (plume center is located at ~10 cm, Figures 4d–4f).

A2. Numerical Experiment

[39] The temperature and velocity fields of an upwelling, laminar, axisymmetric plume in a simulated constant viscosity silicone oil are calculated by the Sepran finite element method [*Cuvelier et al.*, 1986] with a penalty function method for the Stokes equation and streamline upwinding for the heat equation [*Vatteville et al.*, 2009]. Assuming an incompressible, infinite Prandtl number fluid, the governing equations of mass, momentum, and energy are

$$\nabla \cdot u = 0 \tag{A1a}$$

$$\nabla P = \nabla \cdot \eta(\nabla u + \nabla u') + \rho g \tag{A1b}$$

$$\rho C_p \left[\frac{\partial T}{\partial t} + (u \cdot \nabla)T\right] = \nabla(k \nabla T) \tag{A1c}$$

where u is fluid velocity, P is pressure, η is the fluid viscosity, ρ is the density, g is the gravitational acceleration, C_p is the specific heat of the fluid, T is the temperature, k is the conductivity, and the apostrophe indicates the transpose. Calculations are performed in a 2-D axisymmetric cylindrical domain of radius 8.5 cm and height 33 cm. The boundary conditions include no-slip conditions on the bottom and side boundaries and free slip at the top boundary. The side and top boundaries are kept at 20°C. The bottom boundary is also at 20°C, except near the center, where we prescribe an elevated temperature of 60°C across a region 1.25 cm wide to initiate the upwelling plume. Calculations are performed on a variable resolution grid with a minimum spacing of 0.2 mm near the heater and along the lower part of the plume axis, with decreasing resolution toward the top and side boundaries. For further details on the method or choice of boundary conditions see *Vatteville et al.* [2009].

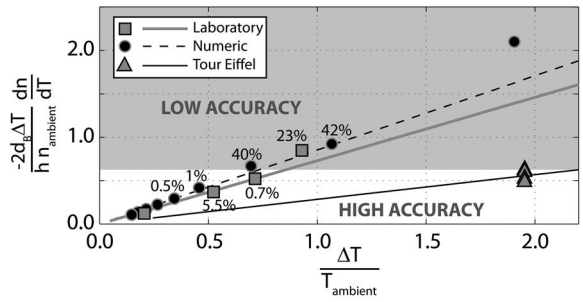

Figure B1. Estimated pixel shifts scaled by the characteristic anomaly size in the laboratory (gray squares), numerical (black circles), and field (gray triangles) experiments are plotted versus the temperature anomaly scaled by ambient temperature. The results indicate that pixel shifts should be kept to values less than 0.65 times the characteristic anomaly size (white region) as indicated by the sharp decrease in error (marked values, from Figure 8a) below this value. The value along the vertical axis varies linearly with temperature anomaly for fixed values of d_B and h in the laboratory (gray line), numerical (dashed line), and field (black line) experiments.

[40] Images are created for the DFV calculation by simulating the apparent background deformation caused by the upwelling plume. The initial, undistorted background image is 30 cm high and 5 cm wide with regularly spaced 0.3 mm diameter black dots at a resolution of 400 dpi which yields images of 4719 × 763 pixels. For each numerical time step, we shoot 3000 by 600 rays through a portion of the simulated temperature field (radius < 2.5 cm) (Figure 1b). Rays are assumed to have a constant ray parameter p,

$$p = \cos(\theta)/n, \tag{A2}$$

where θ is the incident angle of the ray, and n is refractive index of the fluid which is linearly related to temperature in silicone oil (Figure 1d, dn/dT = −3.71e–4 K^{-1}). Raypaths are calculated using a finite difference based marching algorithm with a step size of 0.001 cm. The final positions of the rays are determined 5 cm beyond the center of the plume temperature field. In tests where rays are shot through the interface of two materials of different refractive index, the marching algorithm produces a shift in the final ray position to within 2% of that predicted by Snell's law. A final image is created by displacing the initial image pixels by an amount equal to the change in the ray positions (interpolated to each pixel location) and then interpolating the shifted pixel intensities to the original image coordinates (Figure 4a and auxiliary material). DFV calculations are performed on these images (Figures 4a–4c).

Appendix B: Appropriate Conditions for DFV Measurements

[41] Factors that affect the apparent deformation of an image background include the flow temperature anomaly ΔT (i.e., the size of a refraction index anomaly), the refraction index gradient with temperature $\partial n/\partial T$, and the distance between the camera objective and the anomaly d_B. If a rising refraction index anomaly acts as a thin, divergent lens, then the focal length of the anomaly f_p is given by (Figure 5)

$$\frac{1}{f_p} = \left(\frac{n_{lens}}{n_{ambient}} - 1\right)\left[\frac{1}{R_1} + \frac{1}{R_2}\right], \tag{B1}$$

where n_{lens} is the effective index of refraction of the anomaly (hereafter referred to as the lens), $n_{ambient}$ is the index of refraction of the surrounding fluid, and R_1 and R_2 are the radii of curvature of the lens. We assume that the radii of curvature are equal in magnitude and opposite in sign (i.e., $-R_1 = R_2$) and are approximately equivalent to the characteristic half-width of the anomaly h. In laboratory and numerical experiments, h is the vertical distance between the maximum and ambient temperature in the center of the plume head (laboratory h ~ 0.47 cm, numerical h~0.13 cm). For field measurements (section 5.4), h is defined as the flow parallel distance across significant visible deformation of an anomaly (h~0.39 cm). Substituting h for $-R_1$ and R_2 and the expression for the index of refraction of the anomaly, $n_{lens} = n_{ambient} + (dn/dT)\Delta T$ yields,

$$f_p = \frac{-h n_{ambient}}{2\Delta T\ \partial n/\partial T}. \tag{B2}$$

Using (B2), we estimate the maximum anomaly size at the camera objective by calculating the angle relative to horizontal θ made by a light ray exiting the top of the anomaly lens perceived to come from the focal point of the refraction index anomaly (Figure 5),

$$\Delta p + h = \left(d_B + f_p\right) \cdot \tan(\theta) = \frac{\left(d_B + f_p\right)h}{f_p} \tag{B3}$$

where Δp is the vertical displacement, at the camera objective, of a light ray passing through the top of

the anomaly lens (Figure 5). Substituting (B2) into (B3) and dividing by h yields,

$$\left(\frac{\Delta p}{h}\right) = \frac{-2d_B\Delta T}{hn_{ambient}}\frac{\partial n}{\partial T}, \quad \text{(B4)}$$

a relationship for the scaled apparent background deformation. Based upon our laboratory and numerical experiments, we find that DFV calculations are most accurate for values of $\Delta p/h$ less than ~0.65 (Figure B1).

Appendix C: Image Capture Rate

[42] The ideal image capture rate is a balance between the maximum change in deformation between images and the maximum spatial resolution of the velocity field. In addition, the time between images should be shorter than travel time between individual refractive index anomalies to avoid overlapping deformation at a single location. If a warm, turbulent flow behaves as a series of refractive index anomalies described by

$$n(z) = \sin^2(z), \quad \text{(C1)}$$

where z is the vertical dimension, the maximum change in deformation over a linear displacement ϕ of the fluid is given by

$$\frac{\partial n}{\partial \phi} = \frac{\partial}{\partial \phi}\left(\sin^2(z) - \sin^2(z-\phi)\right) = \sin(2(z-\phi)) = 0 \quad \text{(C2)}$$

which yields a nontrivial shift of $(z - \phi) = \pi/2$, equal to half the distance between anomaly peaks or half the anomaly wavelength. This estimate of the ideal shift is conservative as it assumes a train of closely spaced anomalies. However, it provides a good estimate of the image capture rate required for DFV. The time between image capture Δt_{image} should be equal to or faster than the time a refractive index anomaly travels its characteristic half-width, h (see Appendix B). This yields an image capture rate of

$$\Delta t_{image} = h/V \quad \text{(C3)}$$

where V is the approximate fluid velocity. In the laboratory, numerical, and field experiments examined here, this yields estimates of Δt_{image} = 4.8 s, 1.5 s, and 0.08 s, or 0.21, 0.67, and 12.5 frames per second, respectively. Our actual image capture rates in the laboratory, numerical, and field experiments are 0.5, 1, and 50 frames per second, all faster than the limit estimated by (C3).

Acknowledgments

[43] The authors would like to thank the crew of the research vessel *Pourquoi Pas?* and the pilots of the ROV *Victor 6000* for their aid in collecting the diffuse flow data at the Lucky Strike hydrothermal field. E. Mittelstaedt was supported by the International Research Fellowship Program of the U.S. National Science Foundation (IFRP 0757920), and P. E. van Keken was supported by the U.S. National Science Foundation (EAR-IF 0651056 and EAR-CSEDI 0855487). The Bathyluck'09 cruise was funded by CNRS-INSU/IFREMER. The laboratory experiments were funded by ANR BegDy (project BLAN06-3_145558) to A. Davaille. This project was partially supported by ANR Mothseim (project NT05-3_42213) to J. Escartín. N. Gracias was supported by the Spanish MCINN under the Ramon y Cajal program. This work benefited from discussions with F. Moisy and A. Limare, and the manuscript was improved thanks to the constructive comments of two anonymous reviewers.

References

Baker, E. T., G. J. Massoth, S. L. Walker, and R. W. Embley (1993), A method for quantitatively estimating diffuse and discrete hydrothermal discharge, *Earth Planet. Sci. Lett.*, *118*, 235–249, doi:10.1016/0012-821X(93)90170-E.

Corliss, J. B., M. Lyle, and J. Dymond (1978), The chemistry of hydrothermal mounds near the Galapagos Rift, *Earth Planet. Sci. Lett.*, *40*, 12–24, doi:10.1016/0012-821X(78)90070-5.

Crone, T. J., W. S. D. Wilcock, and R. E. McDuff (2010), Flow rate perturbations in a black smoker hydrothermal vent in response to a mid-ocean ridge earthquake swarm, *Geochem. Geophys. Geosyst.*, *11*, Q03012, doi:10.1029/2009GC002926.

Cuvelier, C., A. Segal, and A. van Steenhoven (1986), *Finite Element Methods and Navier-Stokes Equations*, Dordrecht, Netherlands.

Dalziel, S. B., G. O. Hughes, and B. R. Sutherland (2000), Whole-field density measurements by 'synthetic schlieren,' *Exp. Fluids*, *28*, 322–335, doi:10.1007/s003480050391.

Davaille, A., and A. Limare (2007), Laboratory studies of mantle convection, in *Treatise on Geophysics*, vol. 7, *Mantle Dynamics*, edited by D. Bercovici, pp. 89–165, doi:10.1016/B978-044452748-6.00116-4, Elsevier, Amsterdam.

Davaille, A., A. Limare, F. Touitou, I. Kumagai, and J. Vatteville (2010), Anatomy of a laminar starting thermal plume at high Prandtl number, *Exp. Fluids*, in press.

Edmond, J. M., C. Measures, R. E. McDuff, L. H. Chan, R. Collier, B. Grant, L. I. Gordon, and J. B. Corliss (1979), Ridge crest hydrothermal activity and the balances of the major and minor elements in the ocean: The Galapagos data, *Earth Planet. Sci. Lett.*, *46*, 1–18, doi:10.1016/0012-821X(79)90061-X.

German, C., and K. L. Von Damm (2003), Hydrothermal processes, in *Treatise on Geochemistry*, vol. 6, *The Oceans and Marine Geochemistry*, edited by H. Elderfield, pp. 181–222, Elsevier, Amsterdam.

German, C., A. M. Thurnherr, J. Knoery, J. L. Charlou, P. Jean-Baptiste, and H. N. Edmonds (2010), Heat, volume and chemical fluxes from submarine venting: A synthesis of results from the Rainbow hydrothermal field 36°N MAR,

Deep Sea Res., Part I, *57*, 518–527, doi:10.1016/j.dsr.2009.12.011.

Ginster, U., M. Mottl, and R. P. Von Herzen (1994), Heat flux from black smokers on the Endeavour and Cleft segments, Juan de Fuca Ridge, *J. Geophys. Res.*, *99*(B3), 4937–4950, doi:10.1029/93JB02800.

Gladstone, J. H., and T. P. Dale (1863), Researches on the refraction, dispersion, and sensitiveness of liquids, *Philos. Trans. R. Soc. London*, *153*, 317–343, doi:10.1098/rstl.1863.0014.

Gracias, N. (2003), Mosaic-based visual navigation for autonomous underwater vehicles, Ph.D. thesis, Inst. Super. Tec., Lisbon.

Ingebritsen, S. E., S. Geiger, S. Hurwitz, and T. Driesner (2010), Numerical simulation of magmatic hydrothermal systems, *Rev. Geophys.*, *48*, RG1002, doi:10.1029/2009RG000287.

James, R. H., and H. Elderfield (1996), Chemistry of ore-forming fluids and mineral formation rates in an active hydrothermal sulfide deposit on the Mid-Atlantic Ridge, *Geology*, *24*, 1147–1150, doi:10.1130/0091-7613(1996)024<1147:COOFFA>2.3.CO;2.

Limare, A., I. Kumagai, J. Vatteville, and A. Davaille (2008), Thermal plumes visualisation: Differential interferometry versus thermochromic liquid crystals, paper presented at 13th International Symposium on Flow Visualisation, Univ. of Franche-Comté, Nice, France, 1–4 July. (Available at http://www.ipgp.fr/~limare/318.pdf)

Meier, G. E. A. (2002), Computerized background-oriented schlieren, *Exp. Fluids*, *33*, 181–187.

Quan, X., and E. S. Fry (1995), Empirical equation for the index of refraction of seawater, *Appl. Opt.*, *34*(18), 3477–3480, doi:10.1364/AO.34.003477.

Ramondenc, P., L. N. Germanovich, K. L. Von Damm, and R. P. Lowell (2006), The first measurements of hydrothermal heat output at 9°50′N, East Pacific Rise, *Earth Planet. Sci. Lett.*, *245*, 487–497, doi:10.1016/j.epsl.2006.03.023.

Richard, H., and M. Raffel (2001), Principle and applications of the background oriented schlieren (BOS) method, *Meas. Sci. Technol.*, *12*, 1576–1585, doi:10.1088/0957-0233/12/9/325.

Roesgen, T. (2003), Optimal subpixel interpolation in particle image velocimetry, *Exp. Fluids*, *35*, 252–256, doi:10.1007/s00348-003-0627-8.

Rona, P. A., and D. A. Trivett (1992), Discrete and diffuse heat transfer at ASHES vent field, Axial Volcano, Juan de Fuca Ridge, *Earth Planet. Sci. Lett.*, *109*, 57–71, doi:10.1016/0012-821X(92)90074-6.

Sarrazin, J., P. Rodier, M. K. Tivey, H. Singh, A. Schultz, and P. M. Sarradin (2009), A dual sensor device to estimate fluid flow velocity at diffuse hydrothermal vents, *Deep Sea Res., Part I*, *56*, 2065–2074, doi:10.1016/j.dsr.2009.06.008.

Scheirer, D. S., T. M. Shank, and D. J. Fornari (2006), Temperature variations at diffuse and focused flow hydrothermal vent sites along the northern East Pacific Rise, *Geochem. Geophys. Geosyst.*, *7*, Q03002, doi:10.1029/2005GC001094.

Schultz, A., J. R. Delaney, and R. E. McDuff (1992), On the partitioning of heat flux between diffuse and point source seafloor venting, *J. Geophys. Res.*, *97*(B9), 12,299–12,314.

Schultz, A., P. Dickson, and H. Elderfield (1996), Temporal variations in diffuse hydrothermal flow at TAG, *Geophys. Res. Lett.*, *23*(23), 3471–3474, doi:10.1029/96GL02081.

Sohn, R. A. (2007), Stochastic analysis of exit fluid temperature records from the active TAG hydrothermal mound (Mid-Atlantic Ridge, 26°N): 1. Modes of variability and implications for subsurface flow, *J. Geophys. Res.*, *112*, B07101, doi:10.1029/2006JB004435.

Sutherland, B. R., S. B. Dalziel, G. O. Hughes, and P. F. Linden (1999), Visualization and measurement of internal waves by 'synthetic schlieren.' Part 1. Vertically oscillating cylinder, *J. Fluid Mech.*, *390*, 93–126, doi:10.1017/S0022112099005017.

Töpler, A. (1866), Über die methode der schlierenbeobachtung als mikroskopisches hilfsmittel, nebst bemerkungen zur theorie der schiefen beleuchtung, *Ann. Phys.*, *203*, 556–580, doi:10.1002/andp.18662030405.

Trivett, D. A. (1994), Effluent from diffuse hydrothermal venting: 1. A simple model of plumes from diffuse hydrothermal sources, *J. Geophys. Res.*, *99*(C9), 18,403–18,415, doi:10.1029/94JC00095.

Trivett, D. A., and A. J. I. Williams (1994), Effluent from diffuse hydrothermal venting: 2. Measurement of plumes from diffuse hydrothermal vents at the southern Juan de Fuca Ridge, *J. Geophys. Res.*, *99*(C9), 18,417–18,432, doi:10.1029/94JC00096.

Vatteville, J., P. E. van Keken, A. Limare, and A. Davaille (2009), Starting laminar plumes: Comparison of laboratory and numerical modeling, *Geochem. Geophys. Geosyst.*, *10*, Q12013, doi:10.1029/2009GC002739.

Veirs, S. R., R. E. McDuff, and F. R. Stahr (2006), Magnitude and variance of near-bottom horizontal heat flux at the Main Endeavour hydrothermal vent field, *Geochem. Geophys. Geosyst.*, *7*, Q02004, doi:10.1029/2005GC000952.

Willert, C. E., and M. Gharib (1991), Digital particle image velocimetry, *Exp. Fluids*, *10*, 181–193, doi:10.1007/BF00190388.